

# Fan-noise reduction of data centre telecommunications' server racks, with an acoustic metamaterial broadband, low-frequency sound-absorbing liner



Jack Killeen<sup>a</sup>, Ian Davis<sup>b,c</sup>, Jiayu Wang<sup>a</sup>, Gareth J. Bennett<sup>a,\*</sup>

<sup>a</sup> Department of Mechanical, Manufacturing and Biomedical Engineering, Trinity College Dublin, The University of Dublin, D02 PN40, Ireland

<sup>b</sup> Efficient Energy Transfer (ηET) Department, Nokia Bell Labs, Dublin, Ireland

<sup>c</sup> Segotia Ltd., Ross House, Merchant's Road, Galway City, Ireland

## ARTICLE INFO

### Article history:

Received 29 July 2022

Received in revised form 14 December 2022

Accepted 12 January 2023

### Keywords:

Server rack

Data centre

Telecommunications noise

Occupational noise

Fan noise

Additive manufacturing techniques

Sound power reduction

Acoustic metamaterial

Decorated membrane

Micro-perforated panel absorber

## ABSTRACT

An acoustic metamaterial is evaluated successfully as a means to reduce axial fan noise in an IT server rack application. The continuing growth in demand for cloud-based memory storage is outpacing sustainable energy management which still requires the axial fan as a fundamental component in temperature control technologies. As chip temperatures increase, additional numbers of more powerful fans are required to run faster with the result that data centres have become unsafe working environments due to the acoustic output exceeding prescribed occupational noise level limits. Noise isolation using soundproof cabinets is expensive and impractical in data centres which seek to reduce floor space and communication losses. Instead, in this work, a 15 mm deep acoustic liner solution is proposed being the approach taken in the aeronautics sector to reduce aeroengine noise which, similarly, is a flow duct problem. The acoustic metamaterial adopted here is the recently developed Segmented Membrane Sound Absorber (SeMSA) which can be tailored for low frequency, broadband and tonal noise in a thin form-factor and which can be used in a grazing flow configuration. An equivalent circuit model developed for the SeMSA allows its design to be optimised to attenuate a typical server fan's frequency spectrum. An array of manufactured rectangular SeMSA cells was embedded in a "deflector plate", which is an existing component in a server rack. The deflector plate was implemented in a custom-built fan sound power rig, tested in an hemi-anechoic chamber and compared to a hardwall case and to PU foam. A relative overall decrease of 2.5 dBA was achieved for the SeMSA deflector plate liner which corresponds to a 43.9% decrease in overall sound emissions, which using a material thickness of only 15 mm, signifies an almost twofold increase in the time required for hearing damage to occur. A 3 dBA drop was achieved at the blade passing frequency of 620 Hz, while relative drops of 1–2.5 dBA were achieved from 2000–8000 Hz.

© 2023 The Authors. Published by Elsevier Ltd. This is an open access article under the CC BY license (<http://creativecommons.org/licenses/by/4.0/>).

## 1. Introduction

Occupational noise-induced hearing loss (ONIH) is the most prevalent occupational disease in the world [1–3]. Worldwide, occupational noise exposure is responsible for 16% of cases of disabling hearing loss in adults [4,5]. In the USA alone in 2014, it was estimated that the annual compensation for ONIH was approximately \$242.4 million [6].

Noise exposure limits are enforced by legislation, such as in the US by the Occupational Safety and Health Administration (OSHA)

regulation 1910.95 [7] which limits the maximum exposure to 90 dB(A) for 8 h and requires preventive actions for exposure to 85 dB(A) for 8 h. The European Directive 89/391/EEC [8] is more conservative and limits exposure to 87 dB(A) for 8 h, with lower and higher action levels at 80 dB(A) and 85 dB(A) for 8 h, respectively. Taking these directives into account, the World Health Organisation (WHO) issued a report to determine the noise-induced hearing loss caused by industrial noise emissions [9]. It concluded that, for the two noise levels tested (85–90 dB(A) and > 90 dB(A)), 22 % of workers in the manufacturing sub-sector were exposed to noise levels of 85 dB(A) or higher for this particular statistical population. Preventative measures for controlling high noise levels must be implemented to ensure safer working conditions.

\* Corresponding author.

E-mail addresses: [killeeja@tcd.ie](mailto:killeeja@tcd.ie) (J. Killeen), [ian@segotia.xyz](mailto:ian@segotia.xyz) (I. Davis), [wangj12@tcd.ie](mailto:wangj12@tcd.ie) (J. Wang), [gareth.bennett@tcd.ie](mailto:gareth.bennett@tcd.ie) (G.J. Bennett).

The demand for cloud-based memory storage has grown exponentially during the last decade. According to the International Data Corporation (IDC) in 2020, more than 59 zettabytes (59 trillion GB) of data was consumed in the world [10]. This figure is expected to more than double to 175 ZB by 2025. Currently, air-cooled systems still represent over 95% of data centre facilities, where an often overlooked challenge is acoustic noise emission [11]. The main source of acoustic noise in IT equipment is fans. The European Telecommunications Standards Institute (ETSI) 300 753 [12] has published regulations for the control and minimisation of noise levels emitted from telecommunications-related equipment [13]. As a result, many high-performing telecommunications units are failing the maximum permissible sound power limits which results in delayed release cycles and has a direct impact on productivity and profitability.

There are a number of traditional methods for treating fan noise, however, acoustics experts believe that further gains in the development of quiet fans for air-cooled IT equipment are very difficult to achieve [11]. An alternative approach is to absorb the noise generated while respecting the constraints of server rack and data centre design.

According to the literature, very little research has been published on noise reduction technologies applied to server racks. One particular challenge for the ubiquitous air-cooled system is that as air exchange is required, it is not straightforward to simply enclose each server rack in a soundproof box in a data centre environment. The aeroengine on an aircraft has a similar requirement to allow airflow whilst also attenuating its noise output. The approach commonly adopted for decades with aeroengines is to line the inner surfaces of the nacelle, which are exposed to the acoustic field, with noise-absorbing materials [14–19]. Current developments in aeroengine design are towards the Ultra-High-Bypass-Fan (UHBF) which will result in very large diameter engines. These engines tend to generate lower-frequency tonal and broadband noise. In an attempt to reduce the weight and diameter of the increasingly large engines, the space and depth allocated for the liners have been drastically reduced. The challenge for aeroacousticians is to design liners for lower-frequency and broadband noise in a smaller footprint. As traditional Helmholtz resonator-based, perforated faceplate over honeycomb technologies are unable to satisfy these new objectives, acoustic metamaterials (AMM) are being investigated [20]. The intense activity in this field of AMM research in aeronautics applied acoustics and as published in theoretical and applied physics journals has resulted in a wide range of noise-reducing technologies being developed resulting in a to-date untapped potential for noise absorption in the IT sector.

Recently, [21] first proposed the Segmented Membrane Sound Absorber (SeMSA) design and successfully achieved the attenuation of low-frequency, broadband noise in a light, small form factor. Following this work, [22] proposed the multi-chamber SeMSA design and developed the optimisation algorithm to attenuate fan noise in addition to broadband noise.

The primary purpose of this paper is to achieve the following objectives:

1. To improve the manufacturing strategy for fabricating a SeMSA cell using additive manufacturing techniques and to develop a rectangular version to allow it to be tessellated for more efficient liner design
2. Develop a multi-functional sound power test rig featuring an automated rotation mechanism for high-resolution intensity measurements.
3. To implement a SeMSA liner in a realistic fan-cooled electronics unit modelled on a server rack and to evaluate it as a potential noise reduction technology.

The paper is structured as follows: the SeMSA operating principle is illustrated in Section 2, the experimental rig, facility and procedure is described in Section 3 and the manufacturing strategy for fabricating a SeMSA (Segmented Membrane Sound Absorber) cell suitable for server racks are described in Section 4. The results can be found in Section 5 and finally, the discussion and conclusions are presented in Sections 6 and 7 respectively.

## 2. SeMSA operating principle

A two-chamber SeMSA cell consists of three primary components: segmented air cavities, a Micro-Perforated Panel (MPP) (analysed at length by Maa [23]) and a Decorated Membrane (DM), e.g. [24]. The MPP, which is usually offset from the centre, segments a single, larger air cavity into two smaller cavities of specific depths which are coupled by the perforations in the MPP. An elastic membrane is placed above each cavity and forms a seal over each partition. Rigid platelet masses are adhered to the surfaces of the membranes forming a DM above each cavity.

The operating principle of a SeMSA cell is based on multiple loss mechanisms achieved by the MPP and DM. The system can be described schematically using a solid mechanics model - an example of which is shown in Fig. 1. As incident plane waves impinge on the top surface of the membrane, vibroacoustic behaviour is induced at resonant frequencies which creates pressure acoustic regions in the air cavities. The MPP separating the segments allows control over the damping in the system as the out-of-phase motion of the two membranes causes a pressure differential across the MPP creating airflow through the perforations. This, in turn, creates thermoacoustic regions (shown by the highlighted microperforations in Fig. 1) which result in viscothermal energy dissipation and airflow distortion through the perforations. In our work, although we consider damping due to motion of the membrane, the dominant absorption mechanism is due to the MPP and to facilitate the development of an analytical model, which is absent from other DM work, e.g. that of [25], we examine only the "limp mass" behaviour of the membranes under no tension and whose dynamic response is dominated by their inertial response with negligible membrane stiffness effects. Practically, this means that the added mass must be sized smaller than the cell segment so that there is a latex "hinge" around the mass to ensure limp mass behaviour where, for the first mode, the mass oscillates perpendicular to the membrane with no rotation. The membrane is not pre-tensioned and the dynamic displacement is sufficiently low to minimise stretching in the membrane at the hinge. The significant benefit of this approach with the development of an analytical model is that it lends itself to a less complex optimisation routine than would be possible when considering membrane effects. This routine is then used to determine the optimal SeMSA parameters for maximum absorption. Further details on the SeMSA design and operating characteristics can be found in [21] and [22].

### 2.1. Equivalent circuit analogy

As presented in [21], the SeMSA cell can be modelled using an electrical circuit analogy in the form of an Equivalent Circuit (EC) model which can then allow for analytical analysis. For this dual-cavity cell, the resonant system is formed by two coupled cavities which can be represented by an RLC circuit, as shown in Fig. 2.

The components of the equivalent circuit are represented by their acoustic impedances,  $Z_{m_i}$ ,  $Z_{c_i}$  and  $Z_{MPP}$ . The resonant system for each cavity and its corresponding membrane is represented by the inductor, resistor and capacitor components of the electrical circuit, as shown in Fig. 2, and are characterised by their component impedances;  $Z_{m_i}$  and  $Z_{c_i}$ . For the dual-cavity system shown,

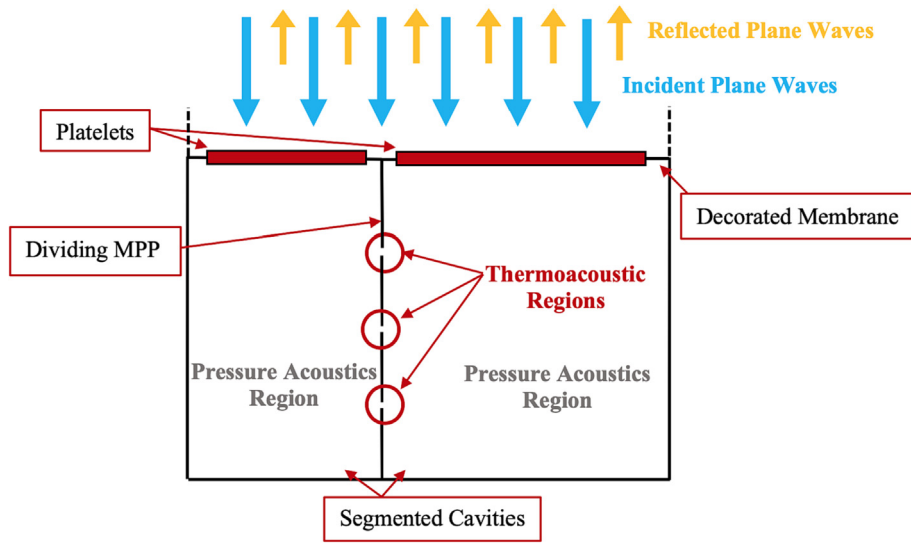


Fig. 1. Solid mechanics schematic for a dual-cavity SeMSA.

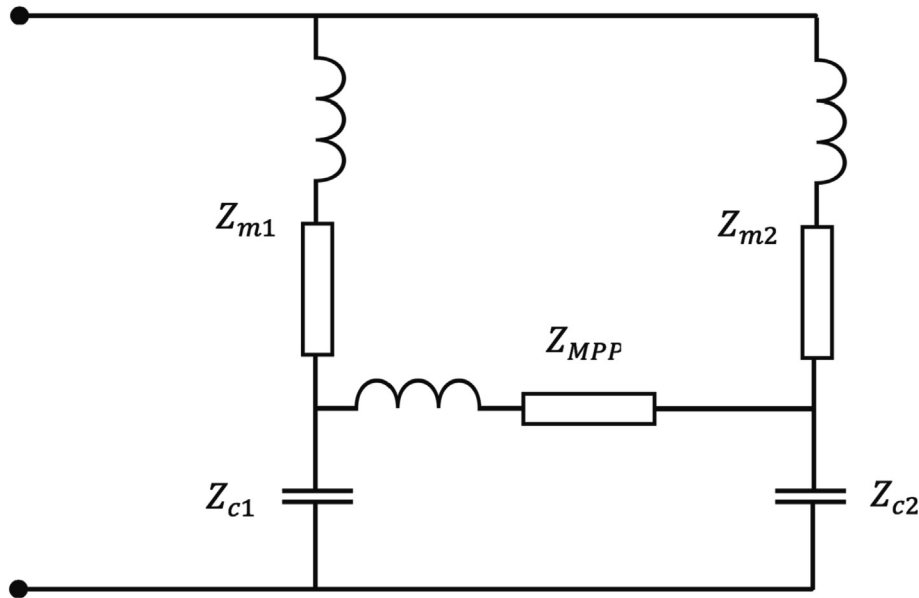


Fig. 2. Equivalent circuit model for a dual-cavity SeMSA cell. Component impedances illustrated.  $Z_m$ : limp-mass membrane impedance,  $Z_c$ : cavity impedance,  $Z_{MPP}$ : micro-perforated panel impedance.

a single MPP couples each resonant system and is also represented by its acoustic impedance,  $Z_{MPP}$ . The equivalent circuit, shown in Fig. 2, employs a lumped element assumption which is valid for  $ka < 1$  where  $a$  is a characteristic dimension.

The acoustic impedances of the limp-mass membranes are given by

$$Z_{m_i} = c_i + j\omega m_i / A_i \quad (1)$$

where  $c_i$  is a damping term,  $m_i$  are the masses of the membrane and added mass, and  $A_i$  is the surface area of the membrane. The impedance of the cavity,  $Z_{c_i}$ , can be defined by the stiffness of the air column as

$$Z_{c_i} = k_{c_i} / j\omega \quad (2)$$

where  $k_{c_i} = \rho_0 c_0^2 / V_i$ ,  $\rho_0 = 1.225 \text{ kg/m}^3$ ,  $c_0 = 343 \text{ m/s}$  and  $V_i$  is the volume of each air cavity. Finally, the acoustic impedance of the MPP,  $Z_{MPP}$ , can be defined using a number of developed models, including

Crandall's model for sound propagation through short, narrow tubes [26] or Maa's approximation [23]. However, to align with the numerical work in this study, the equation used by Version 6.1 of COMSOL Multiphysics [27] for defining the perforated plate boundary condition provides an equation for the specific impedance of the MPP:

$$\frac{Z_{MPP}}{z_0} = -\frac{jk J_0(\frac{d}{2} \sqrt{\frac{-j\omega}{\nu_0}})}{\phi J_2(\frac{d}{2} \sqrt{\frac{-j\omega}{\nu_0}})} [\tau + 0.85d \Psi(\phi)] \quad (3)$$

where  $z_0 = c_0 \rho_0$  and is the characteristic impedance of air,  $k = \omega / c_0$  and is the acoustic wavenumber,  $\nu_0$  is the kinematic viscosity of air,  $d$  is the hole diameter,  $\tau$  is the plate thickness,  $J_0$  and  $J_2$  are Bessel functions, and  $\Psi = \sum_{n=0}^a a_n (\sqrt{\phi})^n$  is the Fok function which accounts for hole-to-hole interaction. By combining the in-series and parallel components of the circuit schematic, the total impedance of the system,  $Z_{EC}$ , becomes

$$z_{EC} = \left( \frac{(Z_{m_1} + Z_B)(Z_{m_2} + Z_C)}{(Z_{m_1} + Z_{m_2} + Z_B + Z_C)} + Z_A \right) (A_1 + A_2) \tag{4}$$

where  $Z_A, Z_B$  and  $Z_C$  are obtained using the  $\Delta - Y$  transform [28], and where multiplying by the total projected area ( $A_1 + A_2$ ) converts from acoustic impedance to specific acoustic impedance. Finally, the absorption coefficient,  $\alpha$ , is calculated by,

$$R_{EC} = (z_{EC} - z_0)/z_{EC} + z_0 \tag{5}$$

$$\Rightarrow \alpha_{EC} = 1 - |R_{EC}|^2 \tag{6}$$

### 2.2. Parameter optimisation

The acoustic performance of a SeMSA cell depends on its specific characteristics such as the cavity depth, plate offset, membrane masses, plate thickness, number of holes/porosity, diameter of the holes, and the membrane damping. As we have developed an analytical model of the SeMSA, we are in a position to optimise the technology by tailoring these parameters to suit the absorption profile of a specific application by maximising the area under the analytical absorption curve using a gradient descent algorithm. An optimisation routine is used for this purpose which uses a cost function to compute the mean sound absorption in a chosen frequency range for a particular cell depth using the total impedance of the system,  $z_{EC}$ . The parameters relating to the cell and MPP dimensions are determined using this optimisation procedure. As the focus of this paper is on developing the SeMSA from a circular cell to a rectangular one, advancing its manufacturability and on applying it to a telecommunications application, the reader is referred to [21],[22] and [31] for further detail on the optimisation procedure.

## 3. Experimental rig for sound power measurements

### 3.1. Server rack imitation

An experimental fan rig was designed to mimic a simplified generic server rack with a forced-air cooling system, such as those found in data centres, for example. However, most server rack

units consist of multiple fans aligned in a tray configuration which can result in quite a complex sound field - especially if subjected to loading effects or a variation in operating speeds. Hence, the designed rig was simplified to a single axial cooling fan with a ducted inlet and free outlet, corresponding to the Type C installation outlined in ISO 13347-3:2004 for measuring fan sound levels. A generic rack unit is shown in Fig. 3a while Fig. 3b presents the design of the simplified unit.

An acrylic housing was built at the outlet section of the fan to imitate the hard-wall chassis of the electronics unit. The deflector plate shown in Fig. 3b is also made from acrylic and imitates the cold-rolled steel deflector plate shown in Fig. 3a. Since the outlet is the primary region of interest due to its open construction, only the upper fan tray is considered and is imitated using a single axial fan. The distance from the fan orifice to the underside of the deflector plate in the acrylic housing roughly matches that of the electronics unit.

Since, in both systems, the deflector plate comprises the largest surface area in the housing configuration and is also likely to be subjected to a high proportion of the fans' energy (due to air-flow/acoustic coupling), this plate was treated with absorptive materials, the "liner", and was designed to be completely removable. Operating fan speeds and deflector angles were chosen to align with the typical values used for cooling these electronic units. However, the operating conditions are not representative of a specific product as this study focuses primarily on proof of concept in a realistic application. A ducted inlet/free outlet configuration was chosen to isolate the outlet section of the rig for analysing sound power at only this location.

### 3.2. Liner test-cases

Two liner test cases were considered in this analysis: a hard-wall deflector plate, which serves as a baseline and a deflector plate lined with sound-absorbing SeMSAs. The setup of each deflector plate is shown in Fig. 4. In each case, the front surface of the plate was positioned at an equal distance from the fan orifice. The hard-wall benchmark consists simply of a 6 mm-thick acrylic panel, while the SeMSA plate houses four individual SeMSA cells.

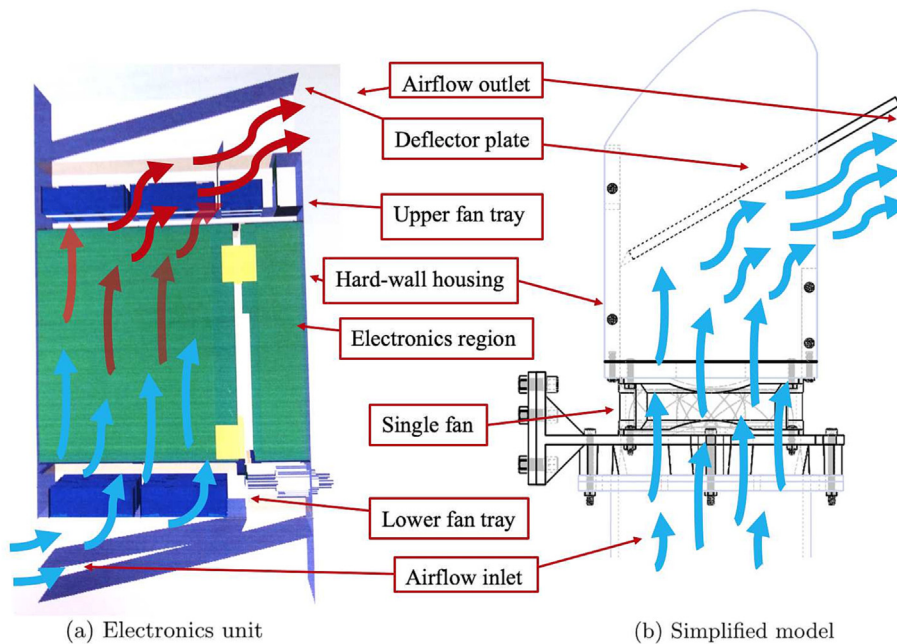


Fig. 3. Generic air-cooled server rack schematic with custom-built imitation model.



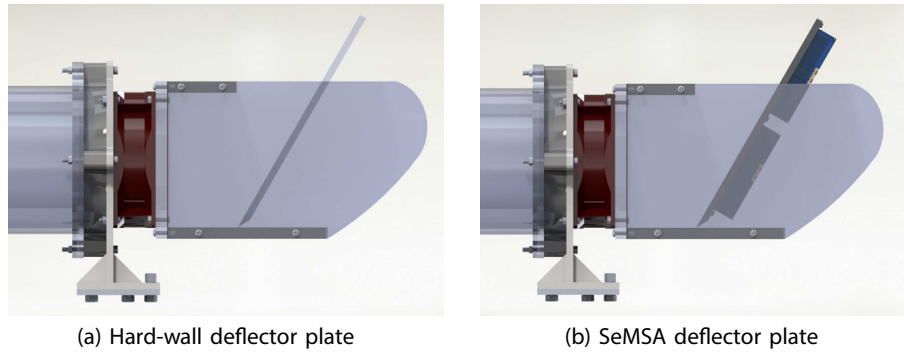


Fig. 4. Deflector plate implementation for (a) hard-wall, and (b) SeMSA test samples.

The edges of the plates are lined with neoprene sponge strips to form a seal between the sides of the deflector plate and the sides of the fan housing. A flexible rubber lip printed using flexible resin is glued to the base of each deflector plate to form a compression seal between the bottom of the plate and the base of the fan housing. Each deflector plate is inserted into the fan housing at an angle measured to the vertical.

Each deflector plate measures  $116.5 \times 200$  mm while the cross-section of the housing measures  $118 \times 118$  mm and was designed to roughly match the diameter of the fan orifice. As shown in both Fig. 4a and Fig. 4b, the top of each deflector plate protrudes out of the acrylic housing. This was done for two reasons: firstly, to physically house a  $2 \times 2$  array of SeMSA cells which are subject to certain size constraints related to the size of the impedance tubes in which they were evaluated, and also to ensure that the top of the plate remains outside the housing in the case of an increased deflector angle.

### 3.3. Microphone measurement positions

The experimental rig was designed and built to ISO 13347-3:2004 specifications for determining fan sound power levels using an enveloping surface method. This method uses a hypothetical measurement surface surrounding the test fan in either parallelepiped, spherical or hemispherical shapes. A hemispherical surface was chosen as the most suitable option given the space and equipment constraints at the time of testing. By creating a hemispherical microphone surface surrounding the test fan, localised sound intensities can be evaluated over each microphone segment

which can be used to determine the overall sound power levels for a particular test setup.

Since a free-field test environment is used (more details provided in Section 3.6), it is possible to create a two-dimensional microphone array along a  $90^\circ$  arc configuration and either rotate the arc or rotate the fan around  $360^\circ$ . In the interest of minimising space and handling cable management, the fan rig assembly was positioned with its outlet at the centre of the hypothetical hemisphere of radius 1.5 m and was rotated through  $360^\circ$  using a turntable bearing. The microphone arc remained fixed and stationary. This enabled measurements at any number of user-defined angular fan positions which were chosen based on the required intensity resolution. The hypothetical microphone surface can be visualised in Fig. 5.

A total of 16 microphones were positioned at equal distances along the microphone arc; with the first and last microphones positioned just offset from the direct top and at the direct base of the hemisphere, respectively. 64 fan positions were used for each rotation, resulting in a hemispherical measurement surface of 1024 individual surface segments. This high number of surface segments creates a hemisphere with a high-intensity resolution for accurate directivity evaluations using a relatively small number of microphones. Fig. 5 displays the individual surface segment associated with each microphone which, in each case, is positioned at the local centre of the respective surface segment. The number of angular fan positions (about the z-axis) was chosen to match the approximate elevation angle between each microphone to the azimuth angle between each rotation position. This helps to achieve relatively proportional surface segments and greatly improves the resolution at the base of the hemisphere.

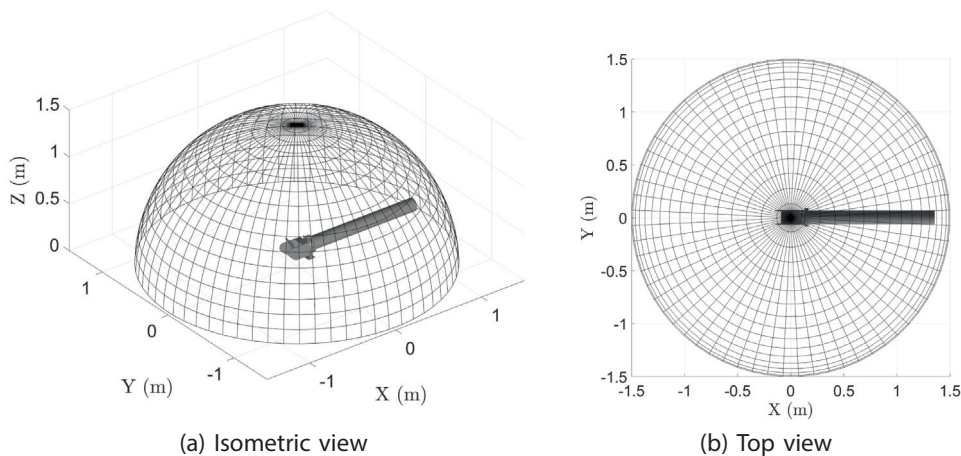


Fig. 5. Wire-frame plot of hypothetical microphone surface segments.

### 3.4. Experimental rig setup

The sound power experimental rig is visually described in Fig. 6. Fig. 6a shows the one-piece aluminium chassis for supporting the microphone and fan rig assembly. Fig. 6b provides a detailed view of the acrylic housing at the fan outlet along with the automated rotation mechanism tasked with rotating it. Fig. 6c provides an annotated model of the entire setup. Photos of the assembly are provided in the Supplementary Materials.

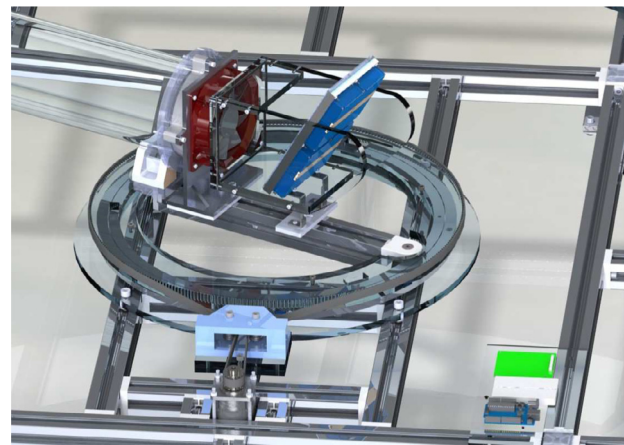
The fan components are fitted to the centre of a circular rotation bearing, with the opening of the fan housing positioned directly below the highest point on the microphone arc. The base plate of the circular rotation bearing remains fixed while the top plate is free to rotate. The top plate consists of a toothed wheel (analogous to a cog or sprocket mechanism) made from acrylic with a pitch of 5 mm and was carefully dimensioned and manufactured using laser-cutting technology. A timing belt - also with a 5 mm

pitch - is wrapped around the rotation plate and fed back to a mid-range bipolar stepper motor which automates the angular positioning of the fan components. A timing belt pulley of equivalent pitch is fitted to the motor shaft while a plastic tensioner with miniature bearing rings (fitted internally) tensions the timing belt to ensure sufficient traction. The motor is programmed to accelerate and decelerate to the next angular position to reduce the required torque for the initial movement.

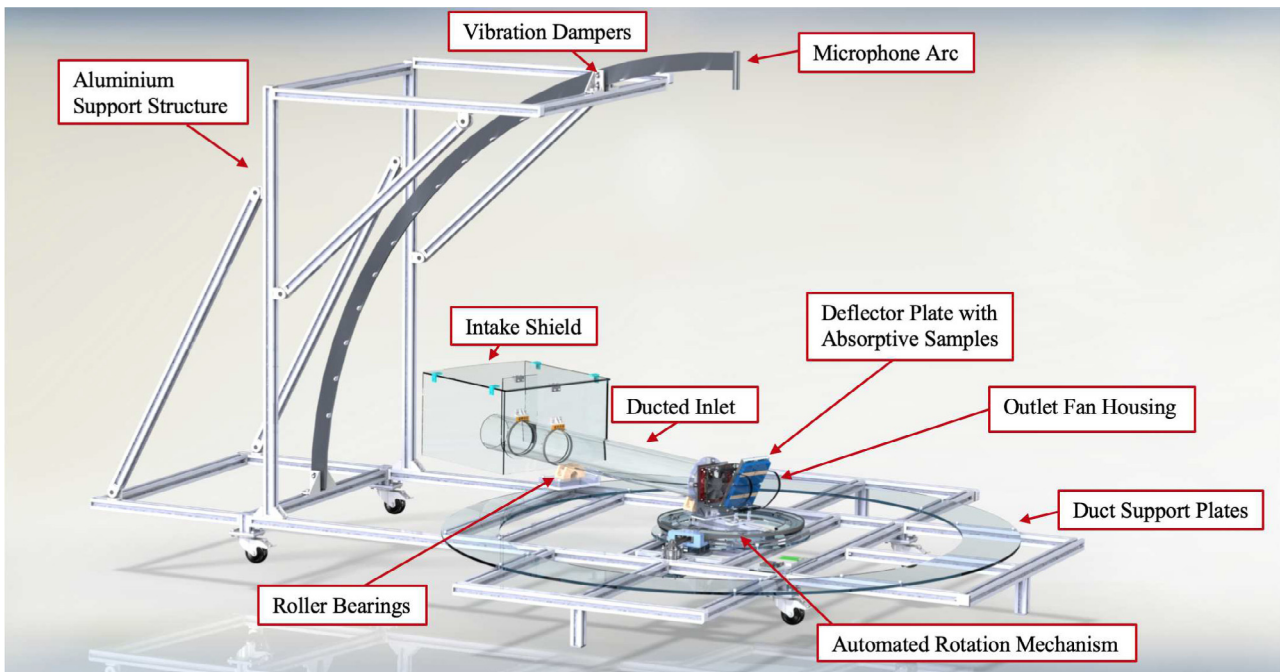
The inlet of the fan test component was isolated using a 1.3 meter-long acrylic duct with an inner and outer diameter of 120 mm and 130 mm, respectively, and was mounted at the inlet side of the fan using a 3D-printed transition part. Ideally, the duct would extend beyond the 1.5 m microphone arc to ensure that only outlet sound power was recorded by the microphones. However, due to space limitations in the test environment, and since the duct needs to rotate through a full 360°, the length of the duct needed to be smaller than the radius of the arc. To compensate for



(a) Aluminium measurement chassis



(b) Automated rotation mechanism



(c) Annotated assembly

Fig. 6. Multiple views of the fan sound power experimental rig setup.

this, an acrylic intake shield (as shown by the duct attachment in Fig. 6c) was designed and positioned at the inlet end of the duct to further assist with inlet–outlet sound isolation. While it does nothing to reduce the component of the sound power recorded at the inlet when the duct is directly in line with the microphone arc, it greatly reduces its effect at the remaining angular duct positions by shielding the inlet from the microphone arc. The duct and shield components are supported through a given rotation using a bearing support system and acrylic support plates.

The wires and cables required for communicating with the microphone sensors, fan system and motor controllers were fed along the inside of the test chamber to the relevant processing equipment outside of the chamber. Insulated BNC connectors and wiring channels in the walls of the chamber were used for this purpose. This was done to reduce the number of possible noise sources and to limit the number of reflective or hard surfaces. Power supplies with internal cooling fans were also placed outside the test chamber.

### 3.5. Instrumentation and test equipment

Sixteen 1/4 inch Brüel & Kjær free-field microphones were positioned equal distances apart along the microphone arc which sampled data at a rate of 48 kHz. The microphones were factory calibrated. Each microphone was fitted with a foam windshield to reduce the effect of turbulent pressure fluctuations or self-noise that may be present in sensors located along the airflow path. Frequency response corrections were applied to each microphone by evaluating the response of the sensor with, and without a fitted windshield subject to a swept sine chirp played through a loudspeaker.

A 120 mm-diameter Sanyo Denki 94 W fan was used throughout the experiments and was controlled using a Pulse Width Modulation (PWM) fan controller. A 1.4A bipolar stepper motor was used to automate the rotating turntable which was driven by a micro-step driver board and controlled by an Arduino UNO [29] using the Arduino software interface.

### 3.6. Test environment

Testing was conducted in the Nokia Bell Labs hemi-anechoic chamber with a hard-surface floor and terminating walls/ceilings which conforms to ISO 13347-3:2004 for evaluating sound power over a reflective plane in a free-field environment. Room impulse response tests were conducted to characterise the acoustic response of the test chamber using reverberation and decay times. The analysis found that the low-frequency cut-off in the chamber under current testing conditions was approximately 300 Hz. Hence, since operating conditions of the current fan setup dictate operating frequencies from approximately 500 Hz upwards, the chamber was deemed sufficiently insulated. The operating conditions within the hemi-anechoic chamber were obtained and are provided in Table 1.

Where  $P_0$  is the air pressure,  $T_0$  is the ambient air temperature,  $\rho_0$  is the air density,  $P_s$  is the static pressure differential at the duct inlet,  $v$  is the rotational speed of the fan and is interpolated from the manufacturer's PWM curve,  $q_m$  is the mass flow rate through the inlet and  $q_v$  is the volumetric flow rate through the inlet. The

density,  $\rho_0$ , was calculated from the room pressure and temperature readings which were obtained using a handheld barometer and thermometer, respectively.  $q_m$  and  $q_v$  were calculated using the measured static pressure differential,  $P_s$ , which was obtained using an additional rig attachment specifically designed for flow rate evaluations (see Supplementary Materials).

Since the operating conditions inside the chamber were unchanging, a measurement time of 10 s for a sample frequency of 48 kHz at each plate position was deemed sufficient for achieving an appropriate frequency resolution. The location of the measurement rig in the anechoic chamber is shown in Fig. 7, where possible, hard surfaces or obstructions in the chamber were treated with foam panels while ensuring the floor beneath the rig remained a hard surface. The entrances to the chamber were kept closed for the duration of each test recording.

### 3.7. Data-acquisition

The NI PXIe-1082 DAQ chassis was used to discretise the recorded voltage analogue signals and convert them to numeric pressure values and was located outside the chamber. BNC cables connect directly to dual 8-channel PXIe slots using shielded Infini-Band connector cables. As mentioned, data is sampled at 48 kHz for a period of 10 s for each recording, resulting in 480,000 data points recorded by each microphone at each angular duct position. The NI MAX driver was used to process the acquired data for further analysis in MATLAB.

## 4. Tessellated SeMSA Panel Absorber

Since the EC model makes no assumption of geometric outline, the SeMSA technology can, in theory, be applied to an arbitrary plan-view shape to suit a particular application. For instance, it is often more useful to work with rectangular or triangular shapes instead of circular shapes, as developed in [21], since these shapes can tessellate and therefore provide a more efficient use of space. Hence, to further develop the technology and to suit the dimensions of the deflector plate, a rectangular SeMSA was designed for testing in the fan sound power experimental rig described in Section 3.

### 4.1. Rectangular SeMSA design concept

The design of the rectangular SeMSA was iterative and needed to be conducted within certain constraints. One geometric constraint was that a single, or set of SeMSAs, needed to tessellate neatly on the deflector plate in rig. A second geometric constraint was that the rectangular SeMSA cell must fit one of the impedance tubes available so that its acoustic absorption coefficient could be evaluated. A coupled geometric-acoustic design constraint was that the outer geometry/size should allow for the acoustic performance required, i.e. to attenuate the noise output from the fan rig. This latter point will be detailed in Section 5.1, A final objective was to develop the SeMSA design from that reported in the [21], not only moving from a circular shape to a rectangular one, but also by improving the manufacturability of the SeMSA using, for example, additive manufacturing where appropriate and a clamping mechanism for the latex membrane.

**Table 1**  
Operating conditions in the anechoic chamber.

$P_0$ (kPa)	$T_0$ (K)	$\rho_0$ (kg/m <sup>3</sup> )	$P_s$ (Pa)	$v$ (min <sup>-1</sup> )	$q_m$ (kg/min)	$q_v$ (m <sup>3</sup> /min)
101.71	299.50	1.18	465	7500	0.39	0.32



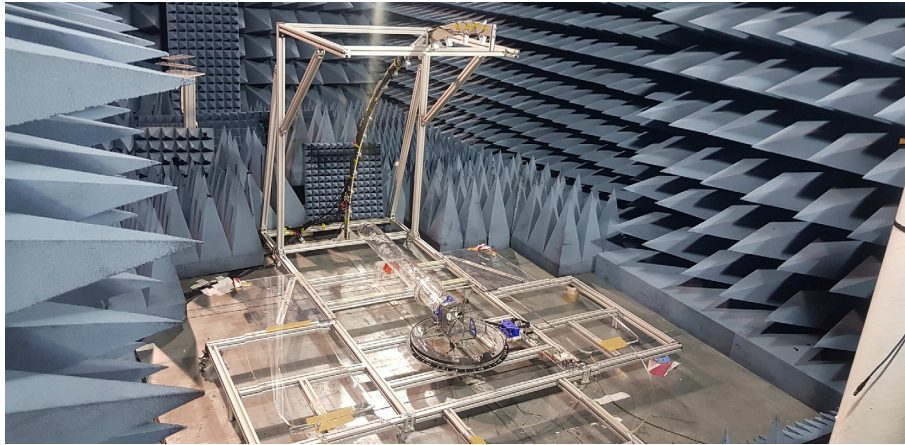


Fig. 7. Location of fan rig in the hemi-anechoic chamber.

Detailed schematics and images of the final design are provided in Fig. 8 and photos in the Supplementary Materials. The main body or shell is printed using the Formlabs Form 2 printer at a 50-micron layer height using the 'Tough' material, which has similar material properties to that of ABS plastic. This material provides slightly better tensile strength than that of the clear resin and is less prone to brittle fracture, as might be associated with the high stresses due to bolt tightening. The MPP resembles an inverted 'T' structure which slots up through the cell from beneath and which bolts into brass inserts glued into the base of the main body, as shown in Fig. 8a. The MPP is fabricated in a similar fashion using Tough resin in the Prusa SL1 printer. The Prusa SL1 printer coupled with a tough resin type is used to fabricate the plate, which is a Digital Light Processing (DLP) method. Unlike SLA printing, it cures a whole layer of liquid resin simultaneously as opposed to localised areas during the polymerisation process. For sub-0.3 mm diameters, the MPP holes were created in two stages.

Initially, pilot holes were 3D printed into the plate to provide the correct location. Using these, the final diameter holes were drilled into the plate with a CNC milling machine to ensure sufficient accuracy and edge quality. For larger diameter holes, adequate accuracy was achieved directly from the print process. A machined brass clamp was used to seal the membrane to the top surface of the main body but was designed with a 2 mm-thick step to slot easily into the deflector plate. Tapped holes are machined into the brass clamp at each corner (and on either side of the MPP) to facilitate membrane clamping. The distance between the cell's internal faces and the screws is maximised to provide sufficient surface area for sealing the latex membrane.

Fig. 8a illustrates the assembly process. Internal cell dimensions are 50 × 80 mm, while a cavity depth of 15 mm was used throughout. A 2 mm fillet was designed at each corner for two reasons: firstly, to match up with the filleted corners in the brass clamp, and secondly, to increase the lateral distance between internal

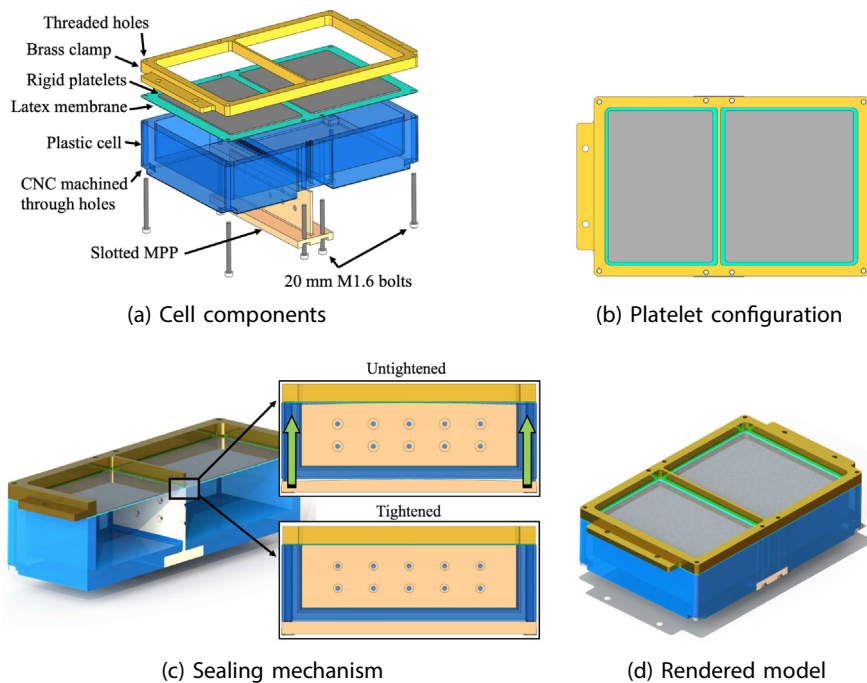


Fig. 8. 15 mm rectangular SeMSA cell design.



faces and clamping screws. While this does intrude on cavity volume, it accounts for less than 1%. A wall thickness of 3.5 mm was applied at the side and end walls of the cavity to ensure that a given cell could be tested in the fan sound power experimental rig, both of which are subject to dimensional constraints. To ensure this wall thickness was sufficient for sound insulation, a 3.5 mm flat plate was printed using the same material and mounted to the impedance tube to evaluate its reflection coefficient experimentally. A reflection coefficient  $\approx 1$  indicated almost complete sound reflection, deeming 3.5 mm a sufficient wall thickness. A base thickness of 5 mm was established to accommodate the 2.5 mm-thick MPP base plate.

Fig. 8b presents the designed platelet configuration. Steel shim metal was used over both cavities in this dual cavity cell and was fixed to the latex membrane using a thin layer of double-sided adhesive tape. This allows the platelet and tape combination to be weighed prior to assembly and ensures accurate mass evaluations. Furthermore, it is important to ensure the shape of the platelet is consistent with the shape of the cavity to achieve the piston-like motion assumed by the EC model. The corners are rounded to match the internal shape of the clamp and shell.

Fig. 8c illustrates the clamping mechanism for sealing the air cavities. The membrane and clamp are first fitted to the plastic shell before the MPP is slotted through the base and secured to the clamp using M1.6 bolts. However, brass inserts are replaced by longer-length bolts fed through the cell walls to connect the MPP directly to the brass clamp. This achieves two things; firstly, it eliminates inserts from the assembly process, which can be awkward to implement, and secondly, it provides additional clamping points close to the centre of the cell for improved sealing at this location. The sides and edges of the slot are again designed with a small sealing lip to form a compressive seal against the MPP.

Due to the increased length of the MPP, and the possibility of slightly misaligned bolt holes, a non-axial load could be introduced which might cause the top edge of the plate to deform, resulting in an air gap between the MPP and the bottom edge of the brass partition. To compensate, the MPP was designed with a small curvature at the top edge of the plate (as shown in Fig. 8c) which ensures it first compresses with the centre of the brass partition before compressing with both ends of the clamp upon tightening which is facilitated by deformation in the plastic. A step was machined into the brass clamp for easy mounting to the deflector plate. Details and photos of the manufactured cell are shown in the Supplementary Materials.

#### 4.2. Deflector plate configuration with grazing flow noise reducing Kevlar.

Four identical, 50 mm  $\times$  80 mm  $\times$  15 mm, rectangular SeMSA cells were inserted into a custom-built plastic deflector plate with built-in steps and slots to match the dimensions of the individual cells, as shown in Fig. 9. Section 3 provides further context regarding the experimental setup of the deflector plate.

Due partly to the masses adhered to the membrane surface, but more to the brass clamp design to fix the membranes in position, the top surface of the SeMSA is not flush. This would not be an issue for normal acoustic measurements but in the grazing flow configuration of the rig, this will result both in additional noise and hydrodynamic pressures on the membrane which would dominate the acoustic pressures for which the membranes are designed to attenuate. In an effort to shield the latex membranes from impinging airflow, two layers of acoustically transparent woven Kevlar were clamped between two additional plates (as shown by the top and base plates in Figs. 9c and 9d) and were flush-mounted to the top surface for reducing aerodynamic noise. To complete the assembly process and render the plate suitable for experimental testing, the sides and ends of the plate were fitted with flexible rubber sealing strips to eliminate potential air gaps. Images of the manufactured and assembled plate are provided in the Supplementary Materials.

### 5. Results

#### 5.1. Normal incidence absorption of rectangular SeMSA

As was stated, the design of the rectangular SeMSA for this application was iterative. Once the outer dimensions of 50 mm  $\times$  80 mm were defined, a depth of 15 mm was chosen, through consultation with Nokia Bell Labs, as being an acceptable depth for the liner. In order to design the characteristics of the SeMSA, the next step was to understand the noise source to be attenuated. This was achieved by measuring the noise output from the experimental rig with the baseline, hardwall deflector plate, as shown in Fig. 4a. The measured spectrum characterising the output noise is shown in Fig. 10. It was obtained by calculating the Power Spectra Density (PSD) with the fan running at 8000 min<sup>-1</sup> and fitted with a hardwall deflector plate. The fan spectrum shown was considered to be typical of one to be attenuated in a data centre.

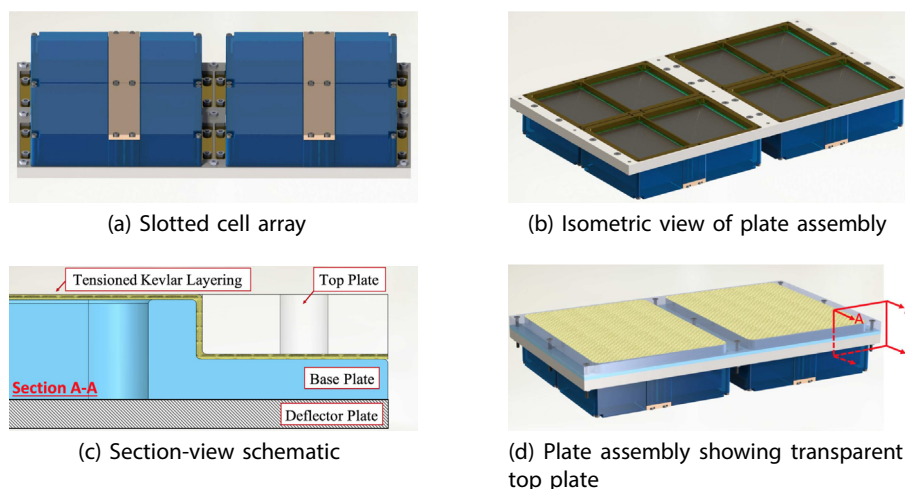


Fig. 9. Model of SeMSA-lined deflector plate with Kevlar attachment plates.

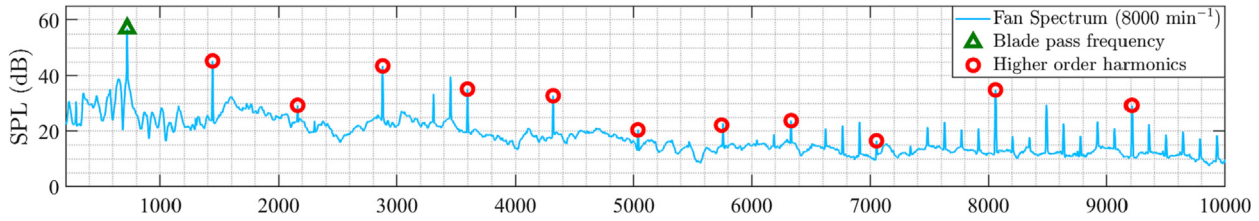
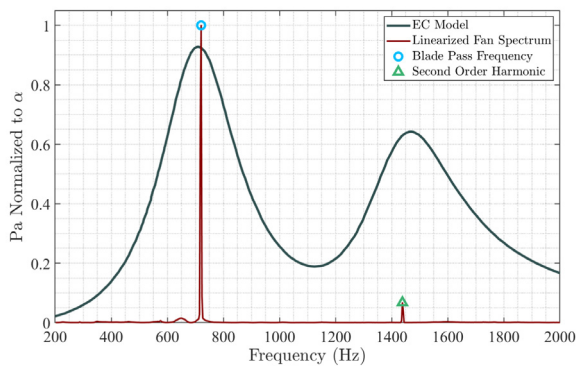


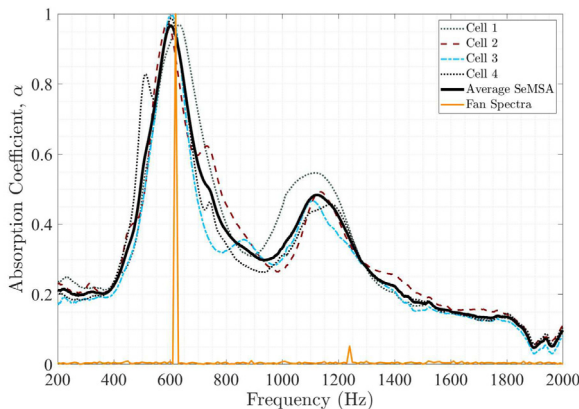
Fig. 10. Fan noise spectrum with baseline, hardwall deflector plate.

The spectrum shows expected broadband noise with a peak at the BPF, located at approximately 720 Hz, with subsequent higher-order harmonics located at integer multiples of the fundamental frequency. Other peaks in the spectrum are related to the shaft speed.

As the BPF, its first harmonic, and the higher level broadband noise is contained within the first 2 kHz, it was decided to optimise the SeMSA to attenuate the noise primarily in this frequency range. Although [21] developed an optimisation routine to allow broadband noise to be attenuated, [22] extended the procedure to allow tonal noise to be targeted also. Fig. 11a shows the predicted sound absorption from the rectangular SeMSA, optimised using the fan spectra up to 2 kHz as the target noise source to be attenuated. The figure also shows the fan spectra plotted in a linear scale and normalised to unity. The results of the optimisation result in a predicted noise absorption of 0.93 at the BPF and 0.64 at the first harmonic.



(a) Initial optimisation result for SeMSA



(b) Experimental Absorption Coefficients for 4 SeMSAs

Fig. 11. Noise source to be attenuated and analytical and experimental SeMSA responses.

Four identical SeMSAs were built according to the procedure detailed in Section 4 and were tested one after the other in a standard normal incidence impedance tube. The experimentally measured absorption curves for the four rectangular SeMSAs are presented in Fig. 11b. Given the potential for variation from one cell to another, the four sets of results are very consistent. However, the frequency response of the cells is not exactly as designed with the peak for maximum absorption being 100 Hz lower than predicted. Better than predicted, however, is the absorption value at the peak which for the average is 0.97, and with some individual SeMSA effectively providing perfect absorption at that frequency. In order to fairly assess the performance of the SeMSA liner, it was decided to reduce the RPM of the fan, to 7500 min<sup>-1</sup>, so as to align the BPF with the maximum absorption peak at 620 Hz. It should be noted that the frequency of the first harmonic no longer perfectly aligns with the secondary absorption peak in the fabricated SeMSA liner and that the absorption value is lower than that predicted by this original EC model.

In order to try and characterise the SeMSAs as made, the shifted fan spectrum was used as the new target spectrum and the result from this optimisation is plotted in Fig. 12 overlaid with the averaged experimental absorption curve. As can be seen, there is a perfect agreement in shape and magnitude at the BPF peak. At other frequencies, the experimental values provide even higher absorption than predicted. The secondary peak is captured by the EC Model but at a slightly lower frequency than predicted. The parameters for an individual SeMSA are provided in Table 2, where  $\delta$  is the plate offset from the geometric centre,  $m_1$  and  $m_2$  are the masses of membrane and added mass over the larger and smaller cavities, respectively,  $\tau$  is the plate thickness,  $d$  is the hole diameter,  $\phi$  is the plate porosity (ratio of micro-perforated area to total area),  $n$  is the number of holes, and  $c_1$  and  $c_2$  are the damping terms associated with the sealed DM at each cavity and are obtained empirically. To be noted here is that the holes, at 1 mm in diameter, are larger than those in the work of [21], as the requirement here is for the attenuation of higher frequencies. This is beneficial as it means the hole diameters are easier to manufacture, such as by 3D printing.

To provide further validation of the EC Model, a 3D COMSOL numerical model of the rectangular SeMSA was developed complete with the upstream rectangular duct of the impedance tube. Two approaches for the impedance of the MPP were examined. The first: COMSOL's interior perforated plate (IPP) boundary condition, employed the impedance model in Eq. 3 as a boundary condition applied to the dividing plate. The second, used COMSOL's thermo-viscous acoustics module (TA) and resolved the holes geometrically in the domain and meshed accordingly. In principle, the latter should be the more accurate approach although it is much more time-consuming to develop and is more computationally expensive to run. The results from the numerical analysis are also presented in Fig. 12. As can be seen, both provide excellent agreement, once again, with the experimental BPF curve. The Numerical TA results agree perfectly with the EC Model, with only a slight frequency shift at the secondary peak for the IPP method. Further

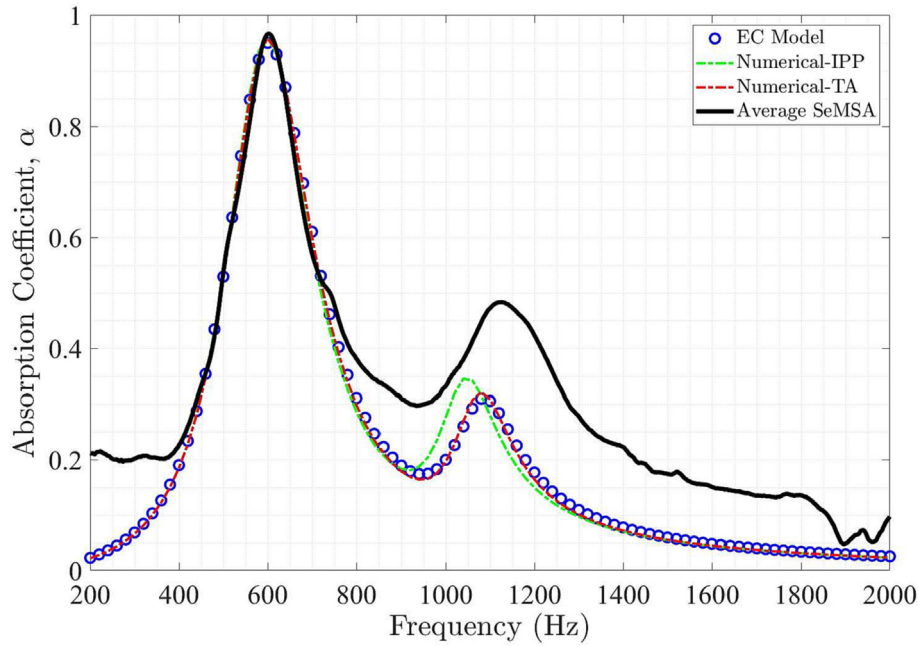


Fig. 12. SeMSA absorption coefficient to target fan noise. Analytical, numerical and experimental results.

**Table 2**  
Optimised material parameters for 15 mm-deep 80 × 50 mm rectangular SeMSA

Sample		Material Parameters							
Depth	Cell ID	$\delta$	$m_1$	$m_2$	$\tau$	$d$	$\phi$	$n$	$c_1$ & $c_2$
15 mm	RP-1,2,3,4	3.93 mm	0.969 g	1.907 g	0.5 mm	1 mm	3.77%	9	$2.7 \times 10^5$

investigation on the differences between the IPP and TA approaches can be found in [21].

A final set of tests was performed in the impedance tube where the absorption coefficient of 15 mm of PU foam was measured. PU foam is considered an industry standard material for noise absorption, but significant depths are required for low-frequency absorption. Fig. 13 provides the results compared to a hard-wall termination and the average SeMSA absorption result. As can be seen, the SeMSA acoustic metamaterial, for the same 15 mm thickness, provides excellent attenuation in the low frequencies compared to the alternatives demonstrating its potential to reduce telecommunications server noise and fan noise in general.

### 5.2. Results of sound power evaluations

Four rectangular cells (named RP-1, 2, 3 and 4 respectively), manufactured according to the parameters in Table 2, were mounted to the sound power experimental rig for evaluating noise levels, as described in Section 3 and in the Supplementary Materials. A hard-wall acrylic deflector plate was used as a benchmark sample and can be visualised in the Supplementary Materials. The test matrix is presented in Table 3. In essence, this analysis prioritises a direct comparison between a completely reflective surface typical of a real rack design and the 15 mm-deep SeMSA cell liner to mitigate fan noise. Hence, only two deflector samples at a single angle are considered in this work. However, the experimental rig permits any number of deflector plate configurations at any angle since plates are completely detachable and can be easily manipulated.

#### 5.2.1. Overall sound power

The sound power analysis was conducted according to the methodologies and equations outlined in Section 3. Overall sound power levels, both unweighted and A-weighted, were calculated using band-filtered surface-averaged sound pressure levels which describe the overall noise levels emitted from the test fan over all frequencies. Sound power,  $P$  (in Watts), was calculated by performing the anti-log of sound power levels,  $L_w$ , using 1pW as a reference. Results for bands below approximately 300 Hz are below the lower cutoff limit of the chamber and were therefore omitted in the calculation of overall levels. The results for each sample are presented in Table 4.

An overall sound power reduction of 2.5 dB was achieved for both unweighted and A-weighted calculations and corresponds to a decrease in sound power of  $3.32 \times 10^{-5}$  W which accounts for an overall reduction of over 43% - a promising result for a material thickness of only 15 mm. Moreover, a 2.5 dB reduction is approximately equivalent to an 800 RPM decrease in fan speed - a reduction of approximately 10.7%. Overall levels can be broken down into third-octave bands for a better understanding of the energy weighting.

#### 5.2.2. Sound power in third-octave bands

Fig. 14 provides the relative differences between the SeMSA and hard-wall deflector plates in band-filtered, A-weighted sound power levels in each third-octave band from 315–20,000 Hz.

A clear and significant reduction of almost 3 dBA is achieved at the 630 Hz third octave band which contains the BPF. Furthermore, additional energy losses of approximately 1–2.5 dBA were identified in the 2000–8000 Hz region which is a positive and

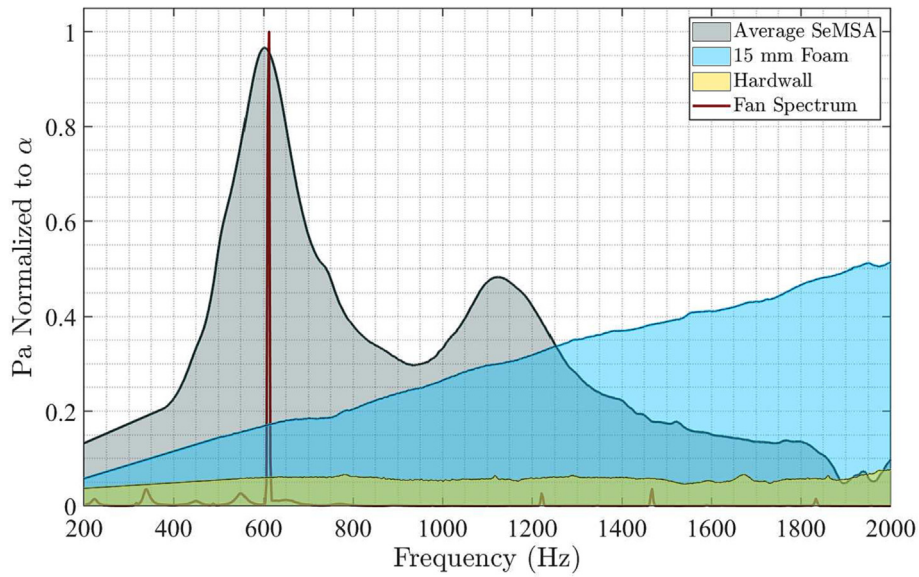


Fig. 13. Performance comparison between hard-wall, foam and SeMSA samples for 15 mm material thicknesses.

Table 3  
Test matrix for sound power evaluations

Test No.	Deflector Sample	Thickness (mm)	Fan Speed ( $\text{min}^{-1}$ )	Deflector Angle ( $^{\circ}$ )	Kevlar Treatment	Total Time (min)
1	Hard-wall	6	7500	35	No	45
2	SeMSA	15	7500	35	Yes	45

Table 4  
Overall sound power.

Config.	$L_w$	$L_{wA}$	$\Delta L_w$	$\Delta L_{wA}$	Sound Power, P	$\Delta P$ (W)	$\Delta P$ (%)
Hard-wall	78.8 dB	77.0 dB(A)	-2.5 dB	-2.5 dB(A)	$7.59 \times 10^{-5}$ W	$-3.32 \times 10^{-5}$	-43.9%
SeMSA	76.3 dB	74.5 dB(A)			$4.26 \times 10^{-5}$ W		

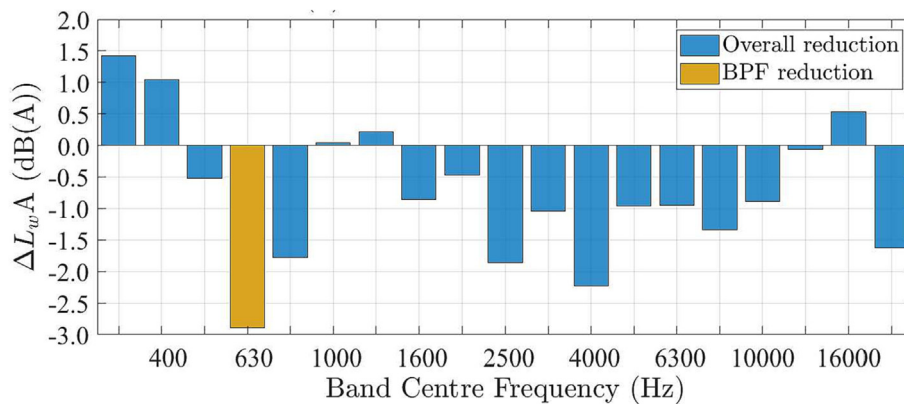


Fig. 14. Sound power levels in third-octave bands for hard-wall vs SeMSA deflector plates.

unexpected result as 2 kHz is above the cut-off frequency of the impedance tube. The relative drop observed at the 4000 Hz frequency band was particularly encouraging. Finally, an increase in sound power at the 315 and 400 Hz third octave bands was identified but is most likely a result of sound reverberations and may not actually represent an increase in acoustic energy.

This arises from the estimation of the chamber cut-off frequency for which 300 Hz was deemed suitable as determined by the room characterisation analysis. In reality, 500 Hz might have been a more reasonable estimate. Regardless, the chamber remains suitable for this analysis since the BPF is entirely contained in the 630 Hz band.



5.2.3. Sound directivity

Band-filtered sound power levels provide invaluable insights into energy levels and weighting. However, they take no account of directivity and assume equal distances (in the case of the hemispherical measurement method) from source to receiver. Hence, a directivity analysis was conducted by producing high-resolution intensity maps using time-averaged SPL measurements generated using the procedures outlined in the Supplementary Materials. Fig. 15 below presents the intensity maps for each sample averaged over all third-octave bands in the 315 Hz - 2 kHz range.

Since the noise radiating from the inlet duct is extraneous, the microphone surfaces (or panels) in this region were visually identified and filtered out by setting them to the average of the local bordering panels. These are illustrated by the enlarged grid lines in Figs. 15b and 15d. The orientation of the fan rig in Figs. 15 is consistent to the orientation displayed in Fig. 5 in Section 3. The colour bar limits for absolute value surface plots were reduced from the maximum and minimum limits to visually highlight performance differences but are consistent for each deflector plate. For relative surface plots, such as those shown in Fig. 16, the colour scaling is performed using the maximum and minimum limits for accuracy purposes.

By comparing Figs. 15a-d a comparison can be made between the hardwall and SeMSA liner as a function of directivity. The overall intensity maps shown in Fig. 15 indicate that a noticeable drop in magnitude (in the region of 3–5 dB) has been achieved between the hard-wall and SeMSA deflector plates. The SeMSA is seen to be particularly effective at reducing noise at localised 'hot spots' which are located around the hemispherical strip at approximately  $z = 1$ . Naturally, intensities are highest at the direct centre of the hemisphere ( $z = 1.5$ ) due to smaller surface areas and, to a lesser degree, floor reverberations. However, absolute values render it

difficult to infer exact energy reductions, and so, a relative intensity map averaged over third-octave bands was generated and is provided in Fig. 16.

Fig. 16 depicts a  $\Delta$ dB range of approximately  $-5$  dB to  $+2$  dB for the SeMSA deflector plate liner relative to the hard-wall plate. Regions of maximum absorption are readily visible. The general conclusion is that for the vast majority of measurement points, the SeMSA leads to a reduction in radiated noise. However, to be noted is an asymmetric behaviour in relative energy reductions between the upper and lower quadrants in the left half of the hemisphere ( $x < 0$ ). To further investigate this, the individual BPF third octave bands was analysed in isolation.

Fig. 17 presents the relative intensity map at the BPF third octave band. Interestingly, the relative intensity plot shown in Fig. 17a exhibits similar directional losses to that shown over the broader frequency spectrum due to the dominance of the BPF. However, the colour bar limits describing relative energy changes at each panel are wider suggesting a larger deviation from the hard wall due to the energy absorption of the SeMSA technology. This clarifies two points: firstly, relative increases or apparent 'no-change' states are, as expected, present in the BPF model as shown by the isolated blue/green panels demonstrating energy increases. Secondly, specific regions or zones with high energy losses can be identified which, in some cases, reach almost  $-8$  dB.

The relative increases are initially considered by addressing three localised pockets around the hemisphere with relative energy spikes of almost 4 dB. These are visualised by the dark-blue panels and, in Cartesian coordinates, are located at approximately  $[-0.4,-0.5,1.4]$ ,  $[0.9,-0.9,1]$  and  $[0.9,0.9,1]$  in Fig. 17a. The latter two locations are symmetrical about  $Y = 0$  and are located above the top left and top right corner of the inlet. Hence, the energy rise is most likely a result of inlet airflow disturbances or

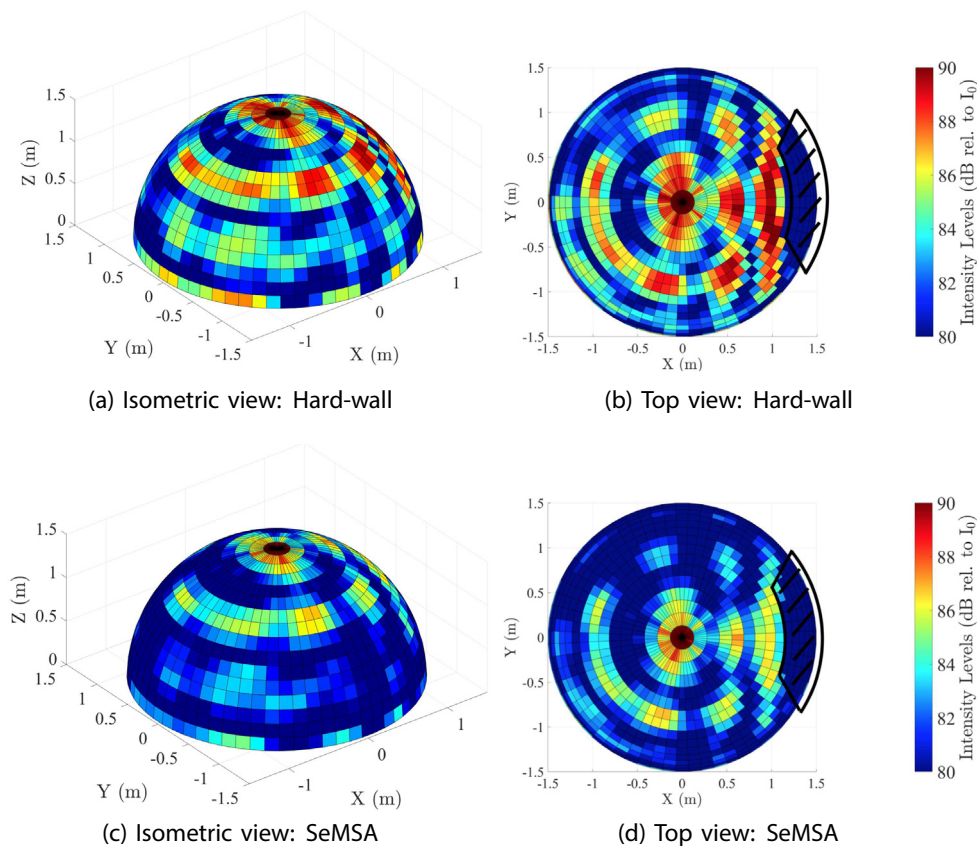


Fig. 15. Hemispherical intensity map averaged over third octave bands.

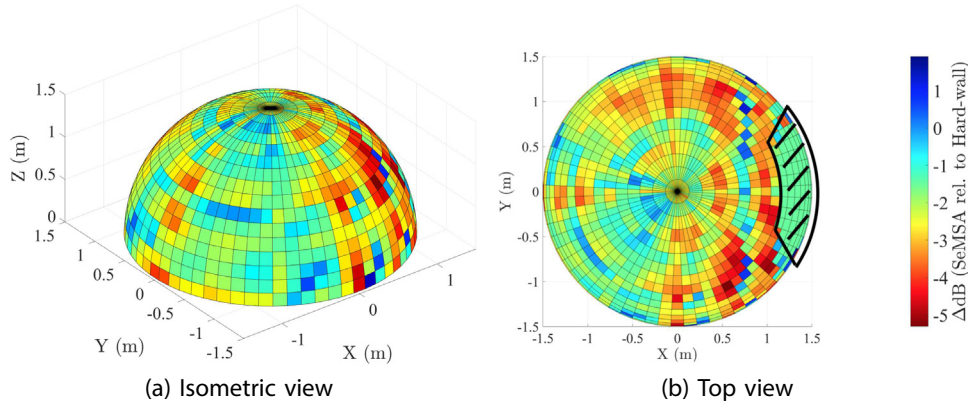


Fig. 16. SeMSA relative to hard-wall intensity map averaged over third-octave bands.

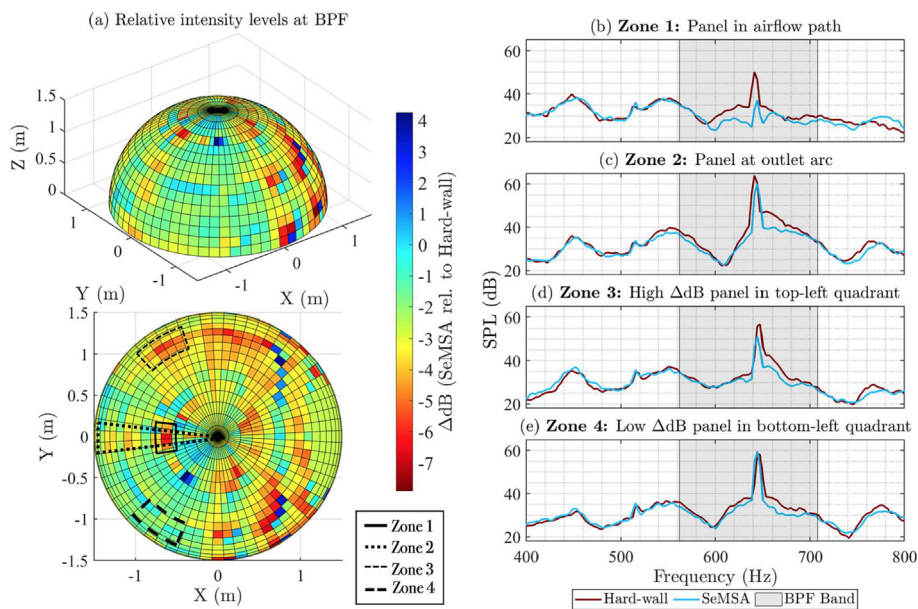


Fig. 17. BPF analysis using relative intensity levels and PSD spectra at four identified zones.

inlet sound energy mistakenly picked up by these microphones. However, the relative increase at  $[-0.4,-0.5,1.4]$  is much more significant. The physical increase itself at the isolated panel is most likely a result of aerodynamic noise generated at the plate boundaries which outweighs the apparent absorption achieved by the SeMSA technology. Its location aligns with the airflow path which renders turbulent pressure fluctuations at the plate boundaries a likely explanation for the relative increase. However, and perhaps more importantly, it highlights an asymmetric energy dissipation between the upper left and lower left quadrants of the intensity map, as seen previously.

To develop a feasible explanation for the apparent asymmetry in the model, four zones exhibiting interesting behaviour were identified and were denoted Zone 1, Zone 2, Zone 3 and Zone 4. Each are located in the highlighted regions in Fig. 17a. PSD averaging for the time-domain signals at a chosen panel in each zone was performed and resulting signals were converted to logarithmic terms for evaluating frequency-weighted SPLs (Fig. 17b - 17e).

Fig. 17b immediately highlights the high BPF energy loss along the airflow path. BPF peak magnitudes dropped by almost 12.5 dB which is a sizeable energy reduction and contributes significantly to the 6.5 dB drop achieved over the entire BPF octave band.

Furthermore, it reinforces the effectiveness of the woven Kevlar treatment which, based on this result, has successfully decoupled the airflow from the sound energy in the region of the BPF. It should be noted, however, that the relative intensity plot averaged over all octave bands (shown in Fig. 16)) de-emphasises the relative drop in the same panel along the airflow path, and so, aerodynamic noise is likely created in other frequencies.

Fig. 17c presents a 4 dB drop in peak magnitude at the BPF for a panel in Zone 2. This zone focuses specifically on the outlet end of the housing and is directly aligned with the deflector plate. Hence, the pockets achieving 3–5 dB losses in this region can be almost directly related to the outlet proportion of the fans sound energy and supports the theory that diffracted waves travelling over and around the deflector plate are successfully treated.

Finally, zones 3 and 4 were analysed in an effort to explain the asymmetric behaviour. Upon examination of the SPL spectra provided in Figs. 17d and 17e, a clear discrepancy was identified in relation to peak magnitudes between symmetric panels. A 5–6 dB reduction was present in Zone 3 while its symmetric equivalent in the Zone 4 panel indicated a relative increase of 0–1 dB, which verified the visual asymmetry identified from the intensity maps.

## 6. Discussion

The SeMSA cells were applied to a realistic fan-cooled electronics unit and tested for evaluating sound power levels, which, as mentioned, equated to a 2.5 dBA reduction. When converted to linear terms, a reduction of just under 44% (in  $W$ ) was achieved which is certainly a notable decrease – especially considering it was achieved by a material with a thickness of just 15 mm. In the context of occupational noise and reducing fan levels, since a 3 dB reduction in sound energy halves the linear sound power which doubles the time it would take for hearing damage to occur, a person could, in theory, work for twice as long under the same conditions [30]. Conversely, for cases where noise levels are currently under control, and considering that a 2.5 dBA reduction equates to an approximate reduction in fan speed of 800 RPM (or 10.7%), the fan speed may even be increased by an equivalent amount to improve thermal performance whilst maintaining the same noise levels.

The strong high-frequency performance from 2000–8000 Hz identified by the band-filtered sound power levels provided in Fig. 14 is a very interesting feature. While not optimised for these frequencies, the SeMSA cells could quite possibly be contributing to additional losses due to the presence of higher membrane eigenmodes, such as, for instance, the 'flapping' motion associated with asymmetric platelet masses [25]. It could however lead to future analytical or numerical work to investigate these findings.

The directivity analysis provided in Section 5.2.3 presents two key findings. Firstly, the intensity maps highlight key locations of acoustic energy fluctuations between the two tested samples. This provides invaluable information about the sound field surrounding the housing and may serve to facilitate further manipulation of the sound field by re-focusing the SeMSA cells to areas with low relative energy drops. The airflow path was a notable location of high energy loss which, crucially, deemed the technology suitable for airflow applications when suitably protected – somewhat of an unknown factor prior to this work. Furthermore, the asymmetric behaviour was most likely a result of either sound leakage through one side of the housing walls or an air-gap/damaged membrane in one (or more) of the cells in the plate array. In the case of the latter, it perhaps magnifies the risks associated with using shallow liner thicknesses with narrowband absorption peaks.

In addition, the averaging procedure performed at the inlet has some associated drawbacks. While the outlet was the primary focus, inlet sound could have been considered in the analysis since a portion of the sound energy is likely reflected back in the direction of the airflow after it had been treated by the deflector plate. If quantifying both inlet and outlet sound energy was deemed important initially, larger overall energy reductions may have been achieved by considering the inlet panels in the analysis. By extension, setting the value of each inlet panel to the average of the bordering panels may be an oversimplification and may in fact be underestimating the performance of the SeMSA technology at this location.

## 7. Conclusions

Specific conclusions and outcomes are summarised as follows:

1. An advanced SeMSA cell manufacturing strategy using additive manufacturing techniques was proposed.
2. A multi-functional sound power test rig was developed featuring an automated rotation mechanism for high-resolution intensity measurements.
3. Rectangular SeMSA cell shapes optimised to a fan noise spectrum were designed and fabricated using the improved manufacturing strategy and were validated experimentally.

4. Four successful cells were applied to a realistic forced-air cooling application for sound power evaluations and source identifications.
5. An overall drop of 2.5 dBA was achieved for the SeMSA deflector plate relative to a hard wall which corresponds to a 43.9% decrease in overall sound emissions and signifies an almost two-fold increase in the time required for hearing damage to occur.
6. A 3 dBA drop was achieved at the blade passing frequency while relative drops of 1–2.5 dBA were achieved from 2000–8000 Hz.
7. A sound directivity analysis identified areas of both significant and negligible energy reductions in an asymmetric form which served to highlight specific locations requiring further treatment.

Future work might involve experimentally assessing the performance of greater cavity depths or multi-channel configurations. For verification of the sound power results, numerical simulations might strengthen the arguments posed. In relation to the test procedure, assessing alternative deflector angles to analyse grazing flow would be a useful addition. Furthermore, narrowing or channelling the flow guide by, for example, building up the sides of the acrylic housing might improve surface contact between the incident sound waves and the absorptive treatment for maximising acoustic energy dissipation.

## CRedit authorship contribution statement

**Jack Killeen:** Investigation, Methodology, Software, Data curation, Visualization, Writing – original draft. **Ian Davis:** Investigation, Conceptualization, Methodology, Software, Data curation, Visualization, Resources, Supervision. **Jiayu Wang:** Software, Visualization. **Gareth J. Bennett:** Methodology, Software, Conceptualization, Resources, Data curation, Funding acquisition, Project administration, Supervision, Validation, Writing - review & editing.

## Data availability

Data will be made available on request.

## Declaration of Competing Interest

The authors declare that they have no known competing financial interests or personal relationships that could have appeared to influence the work reported in this paper.

## Acknowledgements

This research was partly supported by the Irish Research Council Enterprise Partnership Scheme (EPSPD/2017/123), with contributions from Trinity College Dublin, Nokia Bell Labs and the Irish Research Council (IRC). Jiayu Wang is supported by the China Scholarship Council (CSC) – Trinity College Dublin Joint Scholarship Programme.

## References

- [1] Chen K-H, Su S-B, Chen K-T. An overview of occupational noise-induced hearing loss among workers: epidemiology, pathogenesis, and preventive measures. *Environ Health Prev Med* 2020;25:65. <https://doi.org/10.1186/s12199-020-00906-0>. <https://environhealthprevmed.biomedcentral.com/articles/10.1186/s12199-020-00906-0>.
- [2] Śliwińska Kowalska M, Zaborowski K. WHO Environmental Noise Guidelines for the European Region: A Systematic Review on Environmental Noise and Permanent Hearing Loss and Tinnitus. *Int J Environ Res Public Health* 2017;14:1139. <https://doi.org/10.3390/ijerph14101139>.
- [3] Basner M, McGuire S. WHO Environmental Noise Guidelines for the European Region: A Systematic Review on Environmental Noise and Effects on Sleep. *Int J Environ Res Public Health* 2018;15:519. <https://doi.org/10.3390/ijerph15030519>.

- [4] Theakston Frank. *Burden of disease from environmental noise: Quantification of healthy life years lost in Europe*. World Health Organisation: Technical Report; 2011.
- [5] Kerr MJ, Neitzel RL, Hong O, Sataloff RT. Historical review of efforts to reduce noise-induced hearing loss in the United States: History NIH. *Am J Ind Med* 2017;60:569–77. <https://doi.org/10.1002/ajim.22627>.
- [6] Basner M, Babisch W, Davis A, Brink M, Clark C, Janssen S, Stansfeld S. Auditory and non-auditory effects of noise on health. *Lancet* 2014;383:1325–32. [https://doi.org/10.1016/S0140-6736\(13\)61613-X](https://doi.org/10.1016/S0140-6736(13)61613-X).
- [7] OSHA Regulation 1910.95. Occupational noise exposure. Occupational safety and health administration; December; 2019a.
- [8] Directive 2003/10/EC of the European Parliament and of the Council of 6 February 2003 on the minimum health and safety requirements regarding the exposure of workers to the risks arising from physical agents (noise) (Seventeenth individual Directive within the meaning of Article 16(1) of Directive 89/391/EEC); 2019b.
- [9] Concha-Barrientos M, Campbell-Lendrum DH, Steenland K. *World Health Organization, Protection of the Human Environment, Occupational noise: assessing the environmental burden of disease from work-related impairment at national and local levels*. World Health Organization, Protection of the Human Environment, Geneva 2004. OCLC: 743423473.
- [10] S. Wasala, Y. Xue, T. Wiegandt, L. Stevens, T. Persoons, Aeroacoustic noise prediction from a contra-rotating cooling fan used in data center cooling systems, in: AIAA aviation 2021 forum, American Institute of Aeronautics and Astronautics, Virtual Event, 2021. doi:10.2514/6.2021-2313.
- [11] Garimella SV, Persoons T, Weibel J, Yeh L-T. Technological drivers in data centers and telecom systems: Multiscale thermal, electrical, and energy management. *Appl Energy* 2013;107:66–80. <https://doi.org/10.1016/j.apenergy.2013.02.047>.
- [12] ETS 300 753. Equipment engineering (EE): acoustic noise emitted by telecommunications equipment. European Telecommunications Standards Institute; 1997
- [13] EN 300 753, Equipment Engineering (EE); Acoustic noise emitted by telecommunications equipment; 2009.
- [14] Richter C, Thiele FH, Li XD, Zhuang M. Comparison of Time-Domain Impedance Boundary Conditions for Lined Duct Flows. *AIAA J* 2007;45:1333–45. <https://doi.org/10.2514/1.24945>.
- [15] Li X-D, Jiang M, Gao J-H, Lin D-K, Liu L, Li X-Y. Recent advances of computational aeroacoustics. *Appl Math Mech* 2015;36:131–40. <https://doi.org/10.1007/s10483-015-1899-9>.
- [16] Chen C, Li X, Thiele F. Numerical study on non-locally reacting behavior of nacelle liners incorporating drainage slots. *J Sound Vib* 2018;424:15–31. <https://doi.org/10.1016/j.jsv.2018.03.005>.
- [17] Chen C, Li X, Hu F. On spatially varying acoustic impedance due to high sound intensity decay in a lined duct. *J Sound Vib* 2020;483:. <https://doi.org/10.1016/j.jsv.2020.115430>115430.
- [18] Zhao K, Okolo P, Neri E, Chen P, Kennedy J, Bennett GJ. Noise reduction technologies for aircraft landing gear-A bibliographic review. *Prog Aerosp Sci* 2019;112:. <https://doi.org/10.1016/j.paerosci.2019.100589>100589.
- [19] Wang Y, Zhao K, Lu X-Y, Song Y-B, Bennett GJ. Bio-Inspired Aerodynamic Noise Control: A Bibliographic Review. *Appl Sci* 2019;9:2224. <https://doi.org/10.3390/app9112224>.
- [20] Kennedy J, Flanagan L, Dowling L, Bennett GJ, Rice H, Trimble D. The Influence of Additive Manufacturing Processes on the Performance of a Periodic Acoustic Metamaterial. *Int J Polym Sci* 2019;2019:1–11. <https://doi.org/10.1155/2019/7029143>.
- [21] McKay A, Davis I, Killeen J, Bennett GJ. Samsa: a compact super absorber optimised for broadband, low-frequency noise attenuation. *Sci Rep* 2020;10. <https://doi.org/10.1038/s41598-020-73933-0>.
- [22] Davis I, McKay A, Bennett GJ. A graph-theory approach to optimisation of an acoustic absorber targeting a specific noise spectrum that approaches the causal optimum minimum depth. *J Sound Vib* 2021;505:. <https://doi.org/10.1016/j.jsv.2021.116135>116135.
- [23] Maa D-Y. Potential of microperforated panel absorber. *J Acoust Soc Am* 1998;104:2861–6. <https://doi.org/10.1121/1.423870>.
- [24] Yang Z, Mei J, Yang M, Chan NH, Sheng P. Membrane-Type Acoustic Metamaterial with Negative Dynamic Mass. *Phys Rev Lett* 2008;101:. <https://doi.org/10.1103/PhysRevLett.101.204301>204301.
- [25] Mei J, Ma G, Yang M, Yang Z, Wen W, Sheng P. Dark acoustic metamaterials as super absorbers for low-frequency sound. *Nature Commun* 2012;3:756. <https://doi.org/10.1038/ncomms1758>.
- [26] Crandall I. *Theory of vibrating systems and sound*, D. Van Nostrand company; 1954.
- [27] COMSOL Multiphysics, 2023. <https://www.comsol.com/>.
- [28] Morton AH. *Advanced electrical engineering*. London: Pitman; 1966.
- [29] Wikipedia contributors, Arduino uno – Wikipedia, the free encyclopedia, 2022. [https://en.wikipedia.org/w/index.php?title=Arduino\\_Uno&oldid=1077882032](https://en.wikipedia.org/w/index.php?title=Arduino_Uno&oldid=1077882032), [Online; accessed 28-March-2022].
- [30] Health Service Executive (HSE), Occupational Noise Exposure, 2015.
- [31] Wang, J., and Bennett, G. J. "Multi-Chamber Micro-Perforated Panel Absorbers Optimised for High Amplitude Broadband Absorption Using a Two-Point Impedance Method." *Journal of Sound and Vibration*, Vol. 547, 2023, p. 117527. <https://doi.org/10.1016/j.jsv.2022.117527>.